

Emergence of moiré superlattice potential in graphene by twisted-hBN layers

Tianyu Zhang,¹ Chengxin Xiao,² Hongxia Xue,¹ Wang Yao,² and Dong-Keun Ki^{1,*}

¹*Department of Physics and HK Institute of Quantum Science & Technology,
The University of Hong Kong, Pokfulam Road, Hong Kong, China*

²*New Cornerstone Science Laboratory, Department of Physics,
The University of Hong Kong, Hong Kong, China*

(Dated: May 17, 2024)

Moiré superlattices formed in stacks of two or more 2D crystals with similar lattice structures have recently become excellent platforms to reveal new physics in low-dimensional systems. They are, however, highly sensitive to the angle and lattice constant differences between the associated crystals, limiting the range of the material choice and the possible moiré patterns for a given 2D crystal. Here, we present a novel approach to realize an atomically flat substrate with a periodic moiré pattern that can induce the moiré potential on the material on top by van der Waals (vdW) interactions, without suffering from the lattice and angle mismatch. By constructing a twisted hBN (thBN) moiré substrate at an angle of about 1° , we show that the graphene on top, aligned around 15° with the neighboring hBN layers, exhibits typical transport properties under a hexagonal moiré potential, including multiple satellite Dirac points (DPs), Hofstadter butterfly effect, and Brown-Zak oscillations. All features point to the existence of the moiré potential in graphene formed by thBN with $\sim 1^\circ$ twist angle. Further statistical study shows that the twist from a parallel interface between the hBN layers is critical to induce the moiré potential. Our study demonstrates that the thBN moiré substrate can be used to investigate moiré physics in arbitrary materials without being constrained by their lattice constants.

Thanks to the atomically flat and chemically inert surface, the hexagonal boron-nitride (hBN) flakes have widely been used as a substrate or a protective layer to preserve high quality electronic properties of various 2D crystals [1, 2]. Moreover, the hBN layer aligned with graphene has shown the first experimental evidence of the moiré superlattice potential that induces satellite DPs, Hofstadter butterfly effect, and Brown-Zak oscillations [3–9]. The study was soon expended to other moiré systems, especially to twisted 2D crystals that exhibit various new physics, such as correlation effects in twisted graphene layers [10–12], unconventional topological states in twisted transition metal dichalcogenides (TMDCs) [13–15], and more. Most of the relevant studies, however, have primarily focused on creating homo-twisted layers or hetero-layers with similar lattice con-

stants, thereby limiting the range of materials studied in moiré physics and the type of moiré pattern for a given 2D crystal [16, 17].

Recently, twisted hBN (thBN) layers have shown interesting ferroelectric properties [18, 19] that can effectively modify electronic transport through graphene on top [18, 20]. This offers an interesting opportunity to expand experimental access to diverse moiré systems because such a twisted hBN interface was expected not only to have a ferroelectric behavior but also to form a hexagonal moiré pattern that can be induced to the target material on top through van der Waals (vdW) interactions [21]. Since the vdW interaction doesn't suffer from angle or lattice mismatch [22, 23] and the hBN itself is an excellent protection layer for 2D crystals, the thBN moiré substrate can be used to induce moiré potential on target materials while preserving their electronic qualities [21]. Followed by a pioneering theory [21], some studies have shown an experimental evidence of the moiré pattern at the thBN interface by local scanning probe and optical measurements [24–27]. However, a clear transport signature of the moiré potential induced on target material by thBN layers has been absent.

To demonstrate that the moiré potential formed at the thBN interface can be induced to the material on top, we use graphene as the target material because the effect of the moiré potential on graphene has well been established [4–6, 28], making it the most reliable experimental platform to examine the effect of the induced moiré potential. For this, we have fabricated a dual-gated Hall bar composed of Au/Cr/hBN/graphene/thBN/hBN on highly doped silicon substrate by dry pick-up and transfer method [29] and standard e-beam lithography, as schematically shown in the top left inset of Fig. 1a (see Methods). During stacking, we have intentionally rotated neighboring layers by approximately 15° except for the two hBN layers that form the thBN interface (Fig. 1a) to prevent unintentional alignment between hBN and graphene and to ensure that any signature of the moiré potential in our measurements originates from the thBN interface rather than other interfaces. We have made samples with different alignments in thBN interface for comparison. We have fabricated the parallel-stacked thBN interface either by cut-and-stacking two bilayer hBN layers at 58.5° , corresponding to a parallel twist at 1.5° (device P1), or by stacking two nearby

bilayer hBN flakes exfoliated from the same single crystal at 1° (device P2). Secondly, We have also fabricated the anti-parallel stacked thBN interfaces as summarized in Table I. Selecting bilayer hBN ensures a strong modulation of the graphene band structure under the moiré potential, as the moiré strength is expected to exponentially decay with the distance between the thBN interface and graphene [21].

Fig. 1b illustrates the longitudinal resistance R_{xx} of graphene in device P2 in a logarithmic scale at two distinct pairs of the voltage probes indicated in the Fig. 1a. In addition to the main Dirac point (MDP), secondary Dirac point (SDP), tertiary Dirac point (TDP), and quaternary Dirac point (QDP) on both hole and electron sides are clearly visible, with positions at ± 2 V, ± 3.3 V, and ± 5.6 V in top gate voltage (V_{TG}) respectively. The nearly same positions of the multiple resistance peaks across the two pairs of voltage probes, R_{xx1} and R_{xx2} , indicate a highly uniform moiré period across the device region. These multiple DPs, in addition to the MDP, are more clearly visible in a color plot of R_{xx1} versus both V_{TG} and a back gate (V_{BG}) shown in the Fig. 1d, where we can find a quinary Dirac point marked by the orange triangle. It is obvious that the features of R_{xx} originating from higher-order DPs in our devices appear stronger compared to those found in hBN/graphene moiré systems [30, 31], possibly due to different moiré strengths [28] in these two systems. Similar features are shown in device P1 but with fewer number of DPs (see Extended Data Fig. 1).

To confirm that the resistance peaks observed were from the higher-order DPs formed by the moiré potential and to estimate the corresponding charge density, we carried out classic Hall effect measurements under magnetic field of $B = 0.5$ T, which exhibits a clear reversal of the sign of the Hall resistance R_{xy} at MDP and SDPs (Fig. 1c). This reversal distinctly reflects the formation of hole-like and electron-like carriers near these higher-order DPs, indicative of the formation of higher-order Dirac cones in the band structure of graphene. Moreover, using the gate capacitance estimated from the data $C_{TG} = 9.7 \times 10^{11} \text{ cm}^{-2}\text{V}^{-1}$, we found that the position of the SDP ($V_{TG} = \pm 2$ V) yields a density $4n_0$ with $4n_0 = 1.94 \times 10^{12} \text{ cm}^{-2}$ that corresponds to the moiré wavelength of $\lambda = 15.4 \pm 0.1 \text{ nm}$, much larger than the maximum wavelength of 14.2 nm that can be created in hBN/graphene moiré systems but matches well with the moiré wavelength expected for the thBN interface at a twist angle of $\theta = \frac{a}{\lambda} \approx 0.93^\circ$ where a represents the lattice constant of hBN. This estimated value is close to the nominal angle of 1° (device P2) that we aimed during fabrication. The larger moiré wavelength compared to the maximum in graphene-hBN moiré provide further evidence that the observed features in R_{xx} and R_{xy} originate from the thBN interface rather than accidental alignment between graphene and hBN.

The effect of the moiré potential in graphene-thBN heterostructures is further clearly visible in magneto-transport measurements. Fig. 2a,b present the magneto-transport of graphene over the thBN in device P2, which is measured by scanning V_{TG} from $B = 12 \text{ T}$ to $B = -1 \text{ T}$. The conventional quantum Hall effect (QHE) can be clearly identified when the carrier density is close to the MDP but away from the SDP, which is marked by the black dashed straight line originating from the MDP in Fig. 2a. These lines are extracted from the minima in R_{xx} and plateaus in R_{xy} that give the monolayer graphene filling factor $\nu \equiv n\phi_0/B = \pm 2, \pm 6, \pm 10, \dots$ [32], where $\phi_0 = h/e$ is the magnetic flux quantum and h is the Planck's constant. In addition, a similar Landau fan structure arising from the hole-side SDP (hSDP) can also be observed, corresponding to a filling factor $\nu = \pm 2$, denoted by the black dashed line in Fig. 2a. By analyzing the data at various magnetic field strengths in Fig. 2a, Fig. 2c illustrates the positions of $\nu = \pm 2$ for hSDP, represented by R_{xx} minima indicated by red and blue triangles, respectively. Additionally, the Landau fan originating from the electron-side SDP (eSDP) is discernible in Fig. 2a, exhibiting a filling factor $\nu = \pm 2$ and ± 6 . These analogous Landau fan diagrams arising from SDP result from the formation of Hofstadter minibands under strong superlattice modulation [7], indicative of the Hofstadter butterfly spectrum.

To elucidate Hofstadter minibands originating from the moiré potential more distinctly, we plot a longitudinal conductivity $\sigma_{xx} = \frac{\rho_{xx}}{\rho_{xx}^2 + \rho_{xy}^2}$ as a function of n/n_0 and B in Fig. 3a as the minima in the color map can be correlated with energy gaps in the Hofstadter spectrum [8]. By constructing the well-known Wannier diagram [33], Fig. 3b, using the Diophantine relation $\frac{n}{n_0} = t\frac{\phi}{\phi_0} + s$ where $\phi = B/n_0$ is the magnetic flux per moiré unit cell, we can identify a set of Hofstadter minibands. We found that the red solid lines in Fig. 3a represent Landau level gaps originating from the MDP, with a filling factor $\nu = 4(N + \frac{1}{2})$ (N is an integer) while the blue broken lines represent σ_{xx} minima fanning out from the hSDP, eSDP, and hTDP and the black dotted lines indicate energy gaps that cannot be traced back to all DPs and are attributed to replicas of the original Dirac spectra originating from a pure-case magnetic field ($B_{1/q}$) [34]. Around $\phi/\phi_0 = 1/q$, the electron behaves as if it is in zero magnetic field, where Landau levels are quantized in the effective magnetic field $B_{eff} \pm |B - B_{1/q}|$, leading to the observation of local Landau fan signatures marked by the black line in Fig. 3b. These analysis clearly confirm that the moiré potential is induced in graphene.

Finally, we provide another evidence of the moiré-induced feature in graphene, the Brown-Zak oscillation [35–37], in our system. Fig. 4a,b illustrate σ_{xx} and σ_{xy} in device P2 versus ϕ_0/ϕ , displaying clear periodicity in the inverse of the magnetic field, $\Delta(1/B) = \frac{1}{\phi_0 n_0}$. This

periodicity arises from the recursive cloning of the original Dirac spectra when $\phi/\phi_0 = 1/q$, known as the Brown-Zak oscillation. We note the absence of higher-order magnetic Bloch band features with $p > 1$, attributed to the reduced Fermi velocity in the flatter higher-order bands with $p > 1$ [9]. Moreover, this periodicity in $1/B$ enables us to determine the wavelength of the moiré superlattice by $1/n_0 = \frac{\sqrt{3}\lambda^2}{2}$ without relying on gate capacitance information. We estimate the moiré wavelength of $\lambda = 14.6 \pm 0.1$ nm corresponding to a twist angle of 0.98° , very close to the nominal twist angle of 1° in our experiment. This consistency of angles clearly demonstrates that the measured moiré effects in our device originate from the designed thBN interface. We also found that the oscillation persists up to high temperature (Fig. 4c,d) which is the characteristic feature of the Brown-Zak oscillation distinguishing it from the Shubnikov-de Haas oscillations [9, 37].

Having confirmed that the moiré potential is induced in graphene on parallel-stacked thBN layers at around 1° twisting angle (devices P1 and P2), we now discuss the effect of twisting angle and the stacking order of the thBN layers on the moiré potential. As shown in the Table I, we found that there is no clear moiré feature observed in graphene on anti-parallel stacked thBN layers (devices A1-A3). This is consistent with the theoretical expectation [21] and EFM characterization [24] as in the anti-parallel interface, the polarization becomes nearly zero at thBN interface, significantly reducing the strength of the moiré potential. Moreover, even in the parallel-stacking, we found that the twisting angle can neither be too small nor larger than around 1° . At small angle near 0.5° , lattice reconstruction would occur to form AB-BA domains that give rise to ferroelectric switching [18]. This will compete with the moiré pattern in the thBN layers. On the other hand, if the twist angle is too large, the moiré strength is expected to be reduced since the Coulomb potential from thBN exponentially decays with the twist angle [21]:

$$V(\vec{R}, z) \propto e^{-\frac{4\pi\theta|z|}{\sqrt{3}a}}, \quad (1)$$

where \vec{R} is the position vector in graphene, z is the distance between graphene and the thBN interface, θ is the twist angle in thBN, and a is the lattice constant of hBN. Furthermore, a larger twist angle can also weaken the lattice relaxation further [24] and significantly reduce the strength of the moiré potential. Although more controlled experiments are needed because of the difficulties in controlling the twisting angle with a 0.2 - 0.3° precision due to unwanted strain or flake rotation during staking, we have indeed found that the devices P3-P6 that were aligned at a twisting angle near or larger than 1° don't exhibit clear moiré features even when they are parallelly stacked (see Table I and Supplementary for more discussions about the statistics).

Our study clearly demonstrates that the moiré potential created by thBN layer can be induced to the material on top even when the target material is not aligned with the neighboring hBN layer. This study, therefore, can be extended to other 2D materials beyond graphene, irrespective of differences in their crystal constants. Furthermore, the orientation of the moiré potential is determined by the thBN, providing the flexibility to position it at any angle relative to the target material. This flexibility serves as another parameter for engineering the miniband structure. Therefore, the moiré potential created at the thBN interface acts as an ultraflat moiré substrate, offering a novel platform for studying the effects of moiré potential on various 2D materials while preserving their electronic qualities.

METHODS

Device fabrication Graphene and thick hBN (20-40 nm) were exfoliated from the crystals from NGS Naturgraphit and from 2D Semiconductors respectively onto a silicon substrate coated with 285 nm SiO_2 proceed by oxygen plasma [38] in advance, whose thickness is estimated from optical contrast or color under white illumination. The few-layer hBN was exfoliated onto a silicon substrate coated with 90 nm SiO_2 to enhance contrast. SHG measurement was done to determine the layer number more precisely by distinguishing odd and even layers. The vdW pick-up method, using a polydimethylsiloxane (PDMS)/poly(Bisphenol A carbonate) (PC) stamp [29], is employed to assemble flakes into heterostructures, where PDMS is hemisphere dome for continuous and slow contact during stacking [39]. The two flakes in thBN are formed by either cut-and-stack or stacking two nearby flakes. The first method was achieved by mounting a thin (diameter: 50 nm) metal tip on a manipulator and cutting an exfoliated flake to two parts. The second method is taken due to the nearby flakes sharing similar crystal direction.

After stacking the vdW heterostructure, the required gate electrode was deposited with Cr/Au=5/50 nm. Then, 1D electrical contact to graphene [40] was defined by plasma etching (CF_4/O_2 with a flow rate of 100/25 sccm, power: 50 W to etch hBN and O_2 with a flow rate of 5 sccm, power: 100 W to etch graphene), followed by deposition of Cr/Au=5/50 nm. Finally, plasma etching was used to define the Hall bar shape of the devices for transport measurements.

Electric transport measurement The device was placed into a cryogenic system filled with Helium (Lake Shore CRYOGENICS) capable of reaching temperatures as low as about 1.6 K for electric transport measurements. The temperature in all figures is 1.6 k if not specified. The measurements were conducted under a current bias of 10 nA in AC mode. A homemade low-noise

and low-frequency electric measurement system (LLEM) combined with lock-in amplifiers (SR830) were employed to minimize noise during the measurements, with the frequency set at 17.777 Hz. The gate voltages were applied by source meters (Keithley 2400 or DC205).

The work is financially supported by the National Key R&D Program of China (2020YFA0309600) and by the University Grants Committee/Research Grant Council of Hong Kong SAR under schemes of Area of Excellence (AoE/P-701/20), CRF (C7037-22G), ECS (27300819), and GRF (17300020, 17300521, 17309722).

* Corresponding author: dkki@hku.hk

- [1] C. R. Dean, A. F. Young, I. Meric, C. Lee, L. Wang, S. Sorgenfrei, K. Watanabe, T. Taniguchi, P. Kim, K. L. Shepard, *et al.*, *Nature nanotechnology* **5**, 722 (2010).
- [2] K. Zhang, Y. Feng, F. Wang, Z. Yang, and J. Wang, *Journal of Materials Chemistry C* **5**, 11992 (2017).
- [3] M. Yankowitz, J. Xue, D. Cormode, J. D. Sanchez-Yamagishi, K. Watanabe, T. Taniguchi, P. Jarillo-Herrero, P. Jacquod, and B. J. LeRoy, *Nature physics* **8**, 382 (2012).
- [4] L. Ponomarenko, R. Gorbachev, G. Yu, D. Elias, R. Jalil, A. Patel, A. Mishchenko, A. Mayorov, C. Woods, and J. Wallbank, *Nature* **497**, 594 (2013).
- [5] B. Hunt, J. D. Sanchez-Yamagishi, A. F. Young, M. Yankowitz, B. J. LeRoy, K. Watanabe, T. Taniguchi, P. Moon, M. Koshino, P. Jarillo-Herrero, *et al.*, *Science* **340**, 1427 (2013).
- [6] C. R. Dean, L. Wang, P. Maher, C. Forsythe, F. Ghahari, Y. Gao, J. Katoch, M. Ishigami, P. Moon, M. Koshino, T. Taniguchi, K. Watanabe, K. L. Shepard, J. Hone, and P. Kim, *Nature* **497**, 598 (2013).
- [7] G. Yu, R. Gorbachev, J. Tu, A. Kretinin, Y. Cao, R. Jalil, F. Withers, L. Ponomarenko, B. Piot, M. Potemski, *et al.*, *Nature physics* **10**, 525 (2014).
- [8] W. Yang, X. Lu, G. Chen, S. Wu, G. Xie, M. Cheng, D. Wang, R. Yang, D. Shi, K. Watanabe, *et al.*, *Nano letters* **16**, 2387 (2016).
- [9] R. Krishna Kumar, A. Mishchenko, X. Chen, S. Pezzini, G. Auton, L. Ponomarenko, U. Zeitler, L. Eaves, V. Fal'ko, and A. Geim, *Proceedings of the National Academy of Sciences* **115**, 5135 (2018).
- [10] Y. Cao, V. Fatemi, S. Fang, K. Watanabe, T. Taniguchi, E. Kaxiras, and P. Jarillo-Herrero, *Nature* **556**, 43 (2018).
- [11] Y. Cao, V. Fatemi, A. Demir, S. Fang, S. L. Tomarken, J. Y. Luo, J. D. Sanchez-Yamagishi, K. Watanabe, T. Taniguchi, E. Kaxiras, *et al.*, *Nature* **556**, 80 (2018).
- [12] C. Shen, Y. Chu, Q. Wu, N. Li, S. Wang, Y. Zhao, J. Tang, J. Liu, J. Tian, K. Watanabe, *et al.*, *Nature Physics* **16**, 520 (2020).
- [13] K. L. Seyler, P. Rivera, H. Yu, N. P. Wilson, E. L. Ray, D. G. Mandrus, J. Yan, W. Yao, and X. Xu, *Nature* **567**, 66 (2019).
- [14] L. Wang, E.-M. Shih, A. Ghiotto, L. Xian, D. A. Rhodes, C. Tan, M. Claassen, D. M. Kennes, Y. Bai, B. Kim, *et al.*, *Nature materials* **19**, 861 (2020).
- [15] T. Devakul, V. Crépél, Y. Zhang, and L. Fu, *Nature communications* **12**, 6730 (2021).
- [16] F. He, Y. Zhou, Z. Ye, S.-H. Cho, J. Jeong, X. Meng, and Y. Wang, *ACS nano* **15**, 5944 (2021).
- [17] S. Carr, S. Fang, and E. Kaxiras, *Nature Reviews Materials* **5**, 748 (2020).
- [18] K. Yasuda, X. Wang, K. Watanabe, T. Taniguchi, and P. Jarillo-Herrero, *Science* **372**, 1458 (2021).
- [19] M. Vizner Stern, Y. Waschitz, W. Cao, I. Nevo, K. Watanabe, T. Taniguchi, E. Sela, M. Urbakh, O. Hod, and M. Ben Shalom, *Science* **372**, 1462 (2021).
- [20] S. Cao, M. Chen, J. Zeng, N. Ma, R. Zheng, Y. Feng, S. Yan, J. Liu, K. Watanabe, T. Taniguchi, *et al.*, *2D Materials* **10**, 025016 (2023).
- [21] P. Zhao, C. Xiao, and W. Yao, *npj 2D Materials and Applications* **5**, 38 (2021).
- [22] A. K. Geim and I. V. Grigorieva, *Nature* **499**, 419 (2013).
- [23] K. S. Novoselov, A. Mishchenko, A. Carvalho, and A. Castro Neto, *Science* **353**, aac9439 (2016).
- [24] C. Woods, P. Ares, H. Nevison-Andrews, M. Holwill, R. Fabregas, F. Guinea, A. Geim, K. Novoselov, N. Walet, and L. Fumagalli, *Nature communications* **12**, 347 (2021).
- [25] S. Chiodini, J. Kerfoot, G. Venturi, S. Mignuzzi, E. M. Alexeev, B. Teixeira Rosa, S. Tongay, T. Taniguchi, K. Watanabe, A. C. Ferrari, *et al.*, *ACS nano* **16**, 7589 (2022).
- [26] M. Hocking, C. E. Henzinger, S. Tran, M. Pendharkar, N. J. Bittner, K. Watanabe, T. Taniguchi, D. Goldhaber-Gordon, and A. J. Mannix, *arXiv preprint arXiv:2403.09912* (2024).
- [27] Z. Zheng, X. Wang, Z. Zhu, S. Carr, T. Devakul, S. de la Barrera, N. Paul, Z. Huang, A. Gao, Y. Zhang, *et al.*, *arXiv preprint arXiv:2306.03922* (2023).
- [28] J. Wallbank, A. Patel, M. Mucha-Kruczyński, A. Geim, and V. Fal'ko, *Physical Review B* **87**, 245408 (2013).
- [29] P. Zomer, M. Guimarães, J. Brant, N. Tombros, and B. Van Wees, *Applied Physics Letters* **105** (2014).
- [30] X. Lu, J. Tang, J. R. Wallbank, S. Wang, C. Shen, S. Wu, P. Chen, W. Yang, J. Zhang, K. Watanabe, *et al.*, *Physical Review B* **102**, 045409 (2020).
- [31] G. Chen, M. Sui, D. Wang, S. Wang, J. Jung, P. Moon, S. Adam, K. Watanabe, T. Taniguchi, S. Zhou, *et al.*, *Nano Letters* **17**, 3576 (2017).
- [32] Y. Zhang, Y.-W. Tan, H. L. Stormer, and P. Kim, *nature* **438**, 201 (2005).
- [33] G. Wannier, *physica status solidi (b)* **88**, 757 (1978).
- [34] D. R. Hofstadter, *Physical review B* **14**, 2239 (1976).
- [35] E. Brown, *Physical Review* **133**, A1038 (1964).
- [36] J. Zak, *Physical Review* **134**, A1602 (1964).
- [37] R. Krishna Kumar, X. Chen, G. Auton, A. Mishchenko, D. A. Bandurin, S. Morozov, Y. Cao, E. Khestanova, M. Ben Shalom, A. Kretinin, *et al.*, *Science* **357**, 181 (2017).
- [38] Y. Huang, E. Sutter, N. N. Shi, J. Zheng, T. Yang, D. Englund, H.-J. Gao, and P. Sutter, *ACS nano* **9**, 10612 (2015).
- [39] K. Kim, M. Yankowitz, B. Fallahazad, S. Kang, H. C. Movva, S. Huang, S. Larentis, C. M. Corbet, T. Taniguchi, K. Watanabe, *et al.*, *Nano letters* **16**, 1989 (2016).
- [40] L. Wang, I. Meric, P. Huang, Q. Gao, Y. Gao, H. Tran, T. Taniguchi, K. Watanabe, L. Campos, D. Muller, *et al.*, *Science* **342**, 614 (2013).
- [41] A. F. Young, C. R. Dean, L. Wang, H. Ren, P. Cadden-

Zimansky, K. Watanabe, T. Taniguchi, J. Hone, K. L. Shepard, and P. Kim, Nature Physics **8**, 550 (2012).

TABLE I. Overview of thBN devices. The prefix 'P' and 'A' denotes parallel and anti-parallel stacking sequence, respectively.

Device	Layer	Nominal angle	Moiré	Extracted angle
P1	2+2	58.5°	Y	1.07°
P2	2+2	1°	Y	0.98°
P3	2+2	58.7°	N	
P4	3+3	1.6°	N	
P5	1+1	1.5°	N	
P6	1+1	1°	N	
A1	2+2	1.5°	N	
A2	2+2	0.5°	N	
A3	2+2	0.5°	N	

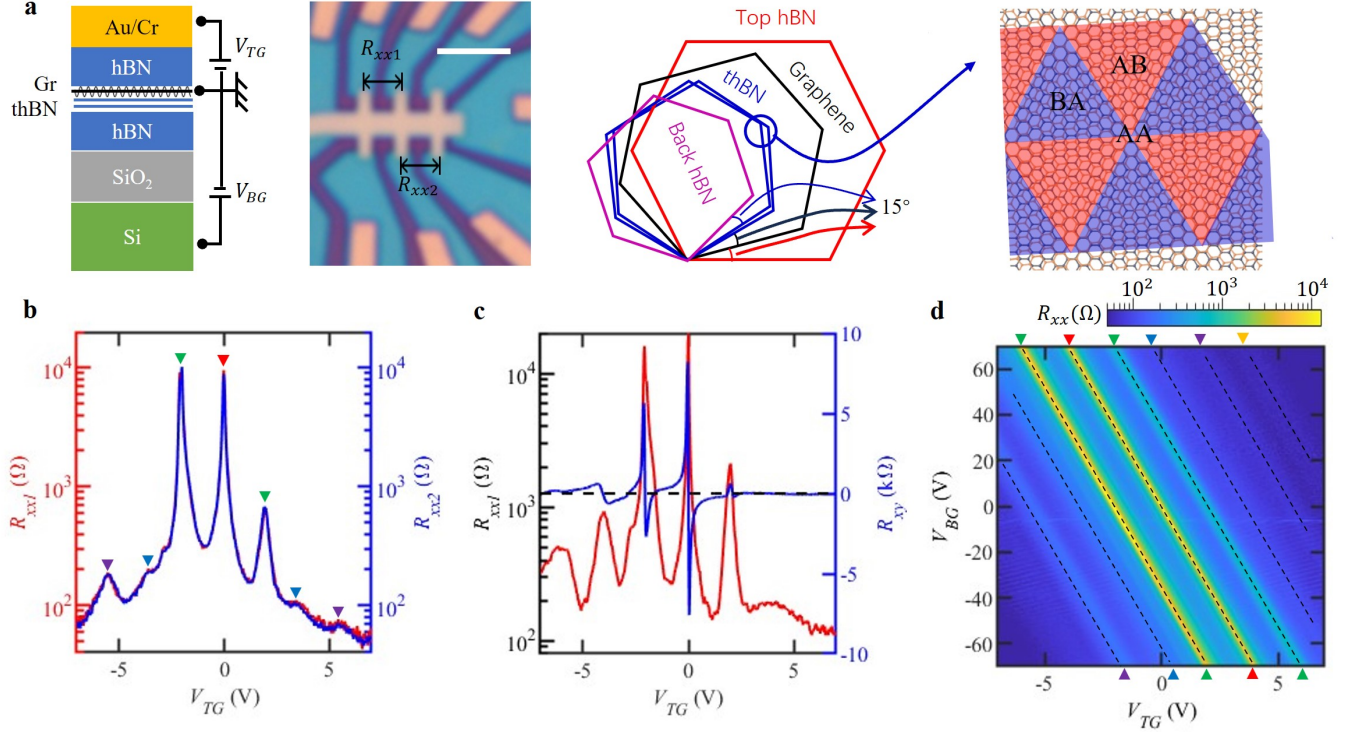


FIG. 1. **Observation of moiré features in graphene on thBN interface (device P2).** **a**, Left: A device schematic where TG denotes a metal top gate and BG represents back gate with highly doped silicon substrate. Middle: An optical image of the device P2 (scale bar: 2 μm). Right: The graphene-hBN alignment in the device and the corresponding hBN stacking order in thBN. **b**, The longitudinal resistance R_{xx1} and R_{xx2} of graphene in a logarithmic scale as a function of V_{TG} at different voltage probes marked in **a**, measured at $T = 1.6$ K and $V_{BG} = 0$ V. Red, green, blue, and purple triangles mark the resistance peaks of R_{xx} at MDP, SDP, TDP and QDP respectively. **c**, Longitudinal resistance R_{xx1} in logarithmic scale (left axis) and Hall resistance R_{xy} (right axis) as a function of V_{TG} at $B = 0.5$ T. The sign of R_{xy} changes at the same gate voltage as the R_{xx} peaks at MDP, SDP and TDP at hole side, confirming that these peaks are from high-order DPs. **d**, A color plot of $R_{xx1}(V_{TG}, V_{BG})$. The black dashed lines mark the position of the DPs at different order.

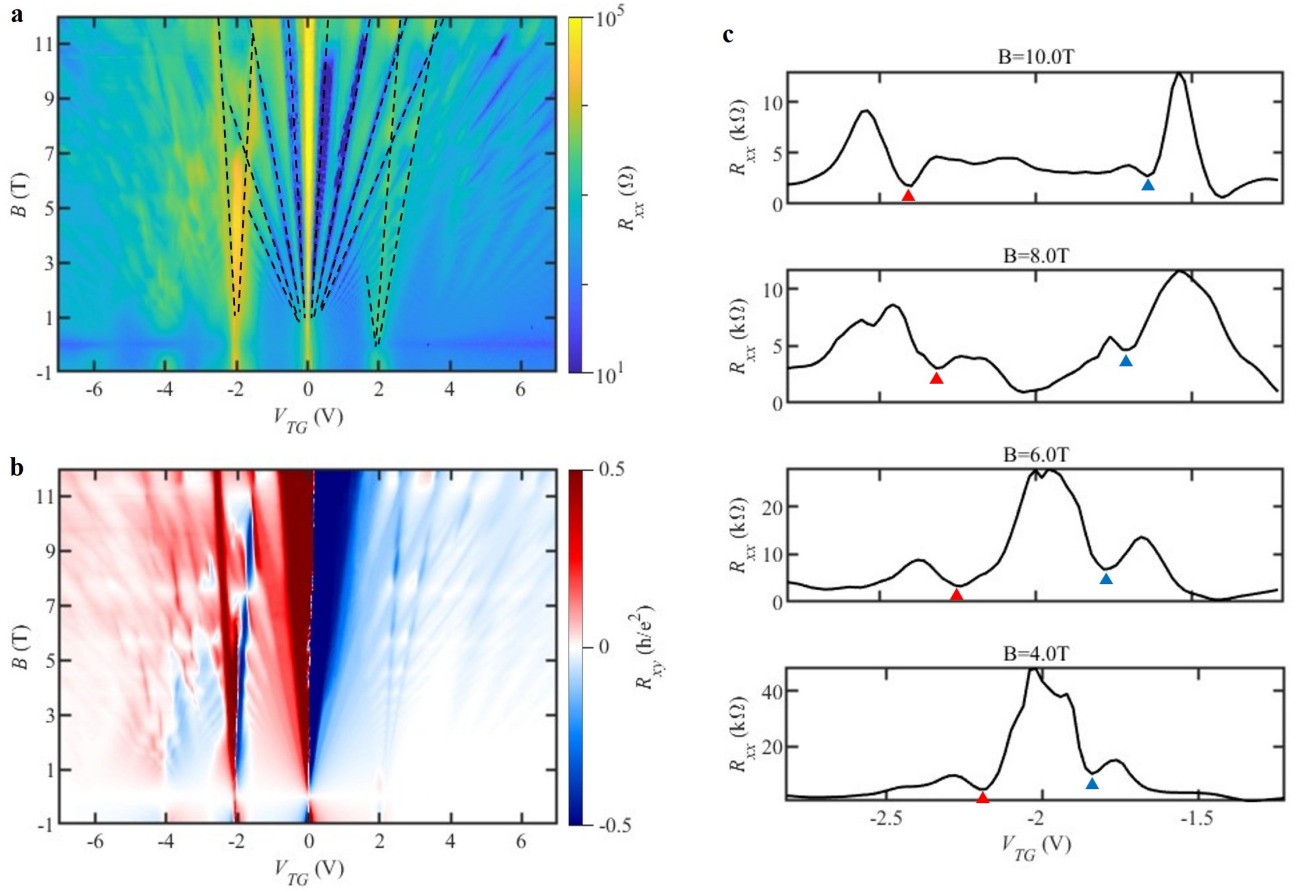


FIG. 2. **Magneto-transport of graphene on thBN.** **a**, A color plot of R_{xx} as a function of a top gate voltage V_{TG} and magnetic field B . The positions of Landau levels are marked by black dashed lines, with filling factors $\nu \equiv \pm 2, \pm 6, \pm 10, \pm 14$ from MDP, $\nu = \pm 2$ from hSDP, and $\nu = 2, \pm 6$ from eSDP. **b**, A color plot of R_{xy} as a function of V_{TG} and B . **c**, 1D cuts of the map in **a**, $R_{xx}(V_{TG})$, near hSDP at $B = 10$ T, 8 T, 6 T, and 4 T, respectively from top to bottom. The red (blue) triangle denotes $\nu = -2(2)$.

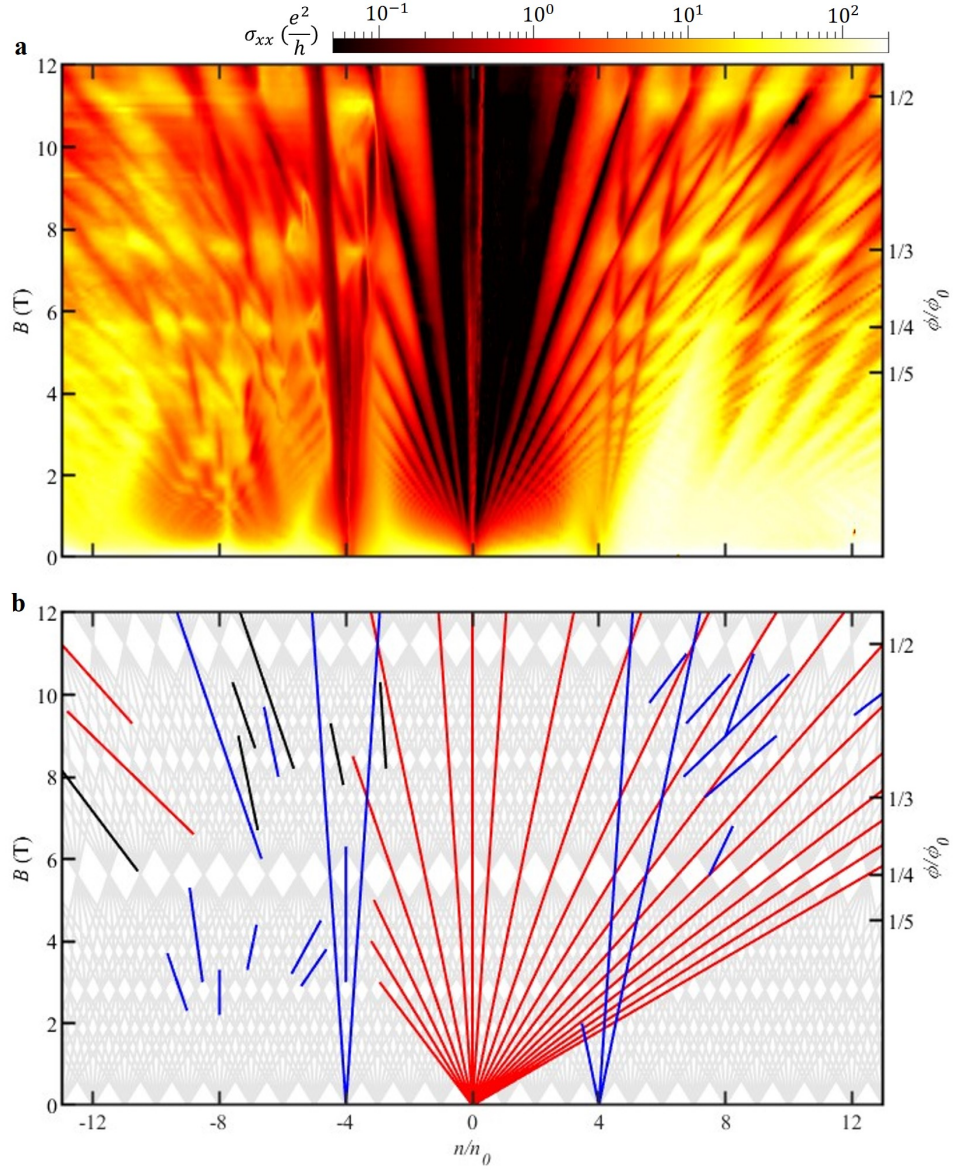


FIG. 3. **Hofstadter butterfly effect.** **a**, Conductivity σ_{xx} as a function of n/n_0 and B , with the right axis indicating the value of ϕ/ϕ_0 , where pure states ($1/q$) are marked on the ticks. **b**, Observed Hofstadter miniband features in Wannier diagram. The gray grid represents the Wannier's grid obtained from the Diophantine relation, $\frac{n}{n_0} = t \frac{\phi}{\phi_0} + s$, indicating the energy gap in the Hofstadter's butterfly. Different colors denote various features in **a**. The red line indicates the expected single-particle gaps with $\nu = 4(N + \frac{1}{2})$ (N is an integer) and the many-body gap $\nu = 0$ originating from the MDP [41]. The blue line represents minima in the σ_{xx} fanning out from hSDP ($s = -4$), hTDP ($s = -8$), and eSDP ($s = 4$) respectively. The black line denotes σ_{xx} minima features fanning out not from all DPs.

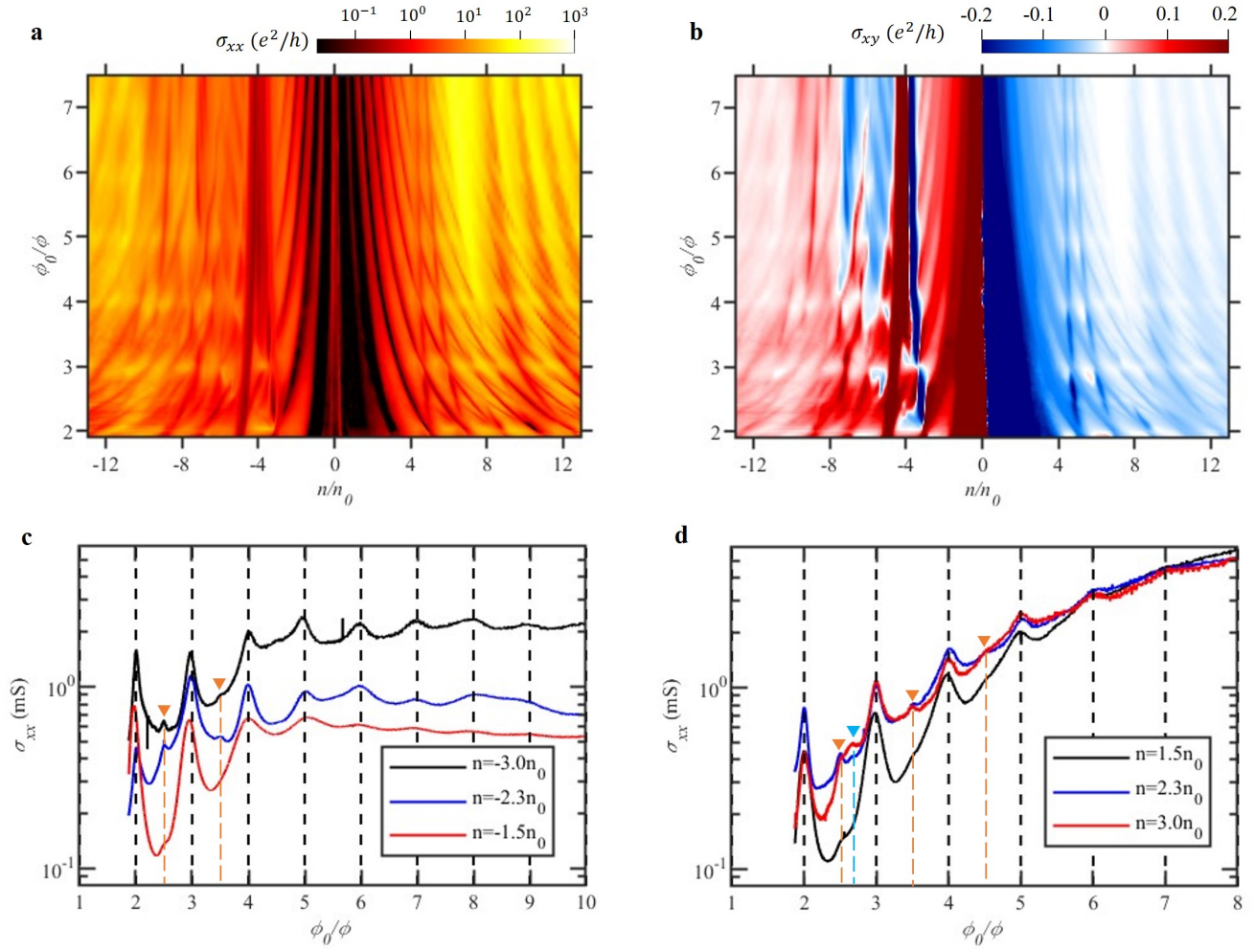
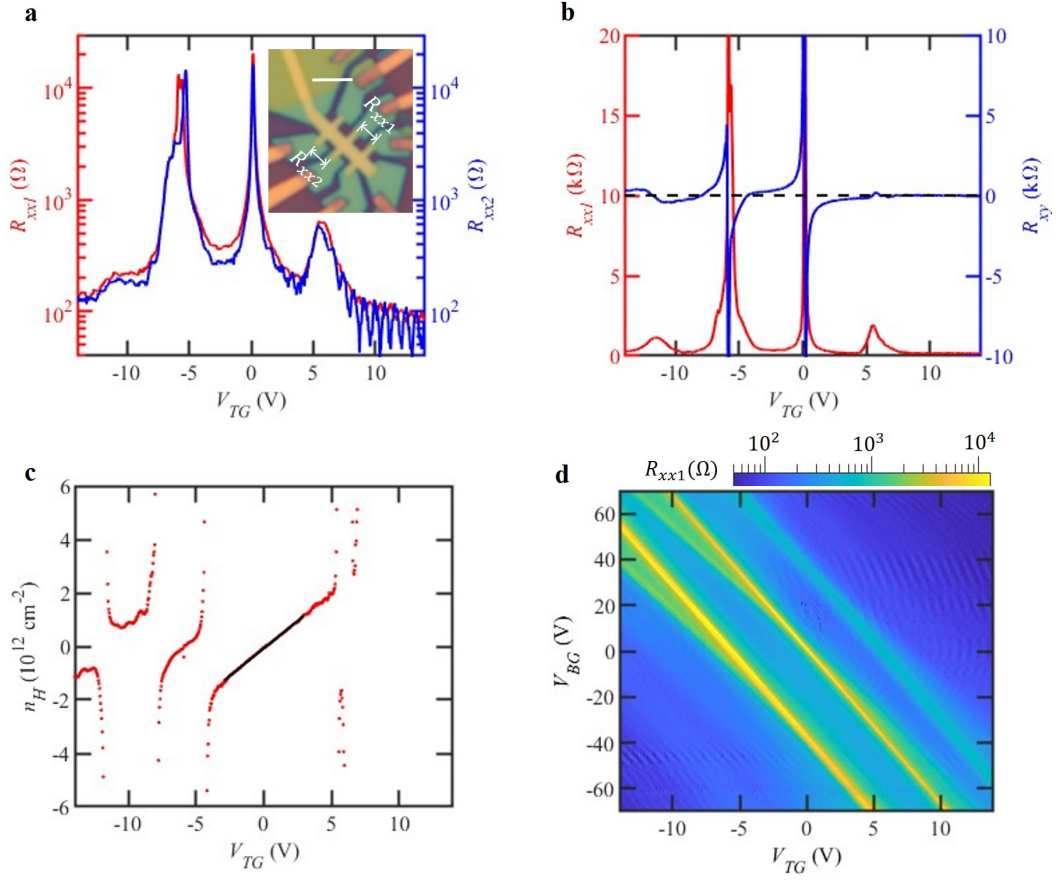


FIG. 4. **Carrier density and magnetic field dependence of Brown-Zak (BZ) oscillations.** **a**, Longitudinal conductivity σ_{xx} as a function of normalized carrier density (n/n_0) and ϕ_0/ϕ measured at 1.6 K, showing periodicity at $\phi_0/\phi = q$. **b**, The same as **a** but measured in Hall conductivity σ_{xy} . **c**, Longitudinal conductivity σ_{xx} as a function of ϕ_0/ϕ in the valence band at $n/n_0 > 1$ measured at 100 K. **d**, The same as **c** with carrier density doping to the conduction band. Black dashed lines mark the position with $p = 1$, while orange and light blue dashed denotes the position with $p = 2$ and $p = 3$, respectively.



Extended Data Figure. 1. **Data from device P1.** **a**, R_{xx1} and R_{xx2} of graphene measured at two sets of probes (marked in the inset) in a logarithmic scale as a function of V_{TG} that exhibits a set of high-order DPs. The inset shows the optical image of the device P1 (scale bar: 2 μm). **b**, R_{xx} (left axis) and R_{xy} (right axis) as a function of V_{TG} at $B = 0.5$ T, displaying the reversals of the sign of R_{xy} at the R_{xx} peaks. **c**, Hall carrier density n_H vs. V_{TG} , where the linear fitting of n_H vs. V_{TG} close to the MDP gives the capacitance of about $4.092 \times 10^{11} \text{ cm}^{-2} \text{V}^{-1}$. **d**, A color plot of R_{xx} as a function of V_{TG} and V_{BG} , showing clear features from high-order DPs.